Torque Ripple Reduction of IPMSM Applying Asymmetric Rotor Shape Under Certain Load Condition

Young-Hoon Jung, Myung-Seop Lim, Myung-Hwan Yoon, Jae-Sik Jeong, and Jung-Pyo Hong, *Senior Member, IEEE*

***Abstract*—This paper proposes a new numerical formula and a design method to reduce the torque ripple while improving efficiency and the control performance of an interior permanent magnet synchronous motor. In previous studies, the inverse cosine function (ICF) has been used for torque ripple reduction by making the air gap flux density distribution sinusoidal under a no-load condition. However, in this paper, the advanced inverse cosine function (AICF) based on the ICF is proposed. It determines an asymmetric rotor shape for rendering the air gap flux density distribution sinusoidal, considering a certain load condition. In addition to the torque ripple reduction, lower peak values, the total harmonic distortion (THD) of the induced voltage, and a lower iron loss can be achieved by applying the AICF, compared to the other conventional methods. The lower peak value and THD of the induced voltage are important because they affect the control performance of the motor. The lower iron loss can also lead to a higher efficiency, particularly, in the high-speed region. To verify the validity of the proposed design method, the characteristics of 8-pole, 12-slot motors that have different rotor shapes are analyzed using finite element analysis and experiments.**

***Index Terms*—Advanced inverse cosine function (AICF), concentrated flux-type synchronous motor (CFSM), eccentric rotor shape, inverse cosine function (ICF), interior permanent magnet synchronous motor (IPMSM), magneto motive force (MMF), torque ripple.**

I. Introduction

UNLIKE the surface-mounted permanent magnet synchronous motor (SPMSM), the interior permanent magnet synchronous motor (IPMSM) in which permanent magnets are embedded in the rotor has the advantage of being structurally strong without the help of other devices and has a small equivalent air gap. In addition, as the inductance of the *d*-axis is different from that of the *q*-axis, both the magnetic torque and the reluctance torque can be used; thus, the power density is higher than that of the SPMSM. Based on these advantages, various applications for vehicles such as electric power steering motors and traction motors have been developed [1]. However, the reluctance torque used to meet the high power density requirement leads to an inevitable torque ripple. As the torque ripple affects the vibration and noise, it should be reduced [2], [3], and [15].

Currently, two main methods for reducing the torque ripple are being investigated [4]. One of them is from the control point of view [5]–[8], while the other achieves an optimal design by changing the shape of the motor. In this paper, only the design methodology is discussed.

Various methods for reducing the torque ripple from the design point of view are being studied. The torque ripple can be reduced by using a notch or a chamfer that reduces the cogging torque [9], [10], and [13]. In addition, changing the arrangement of the permanent magnets or changing the pole-arc can reduce the torque ripple [11]–[14]. In studies [11]–[13], the torque ripple was reduced by placing the permanent magnets in a V-shape. In [13] and [14], the torque ripple was reduced by adjusting the pole-arc. In [15] and [16], the torque ripple was reduced using the skew. In [17], [18], the torque ripple was reduced by making the air gap magnetic field distribution sinusoidal through the application of an eccentric rotor shape. In [19] and [20], the torque ripple was reduced by changing the rotor shape using the inverse cosine function (ICF). In particular, in [19], the total harmonic distortion (THD) of the air gap flux density was compared after applying the ICF and an eccentric rotor shape. This can reduce the torque ripple by making the air gap magnetic field distribution sinusoidal. However, as these methods consider only the no-load condition, the effect of the armature reaction under a load condition has not been considered.

In this regard, this paper proposes the advanced inverse cosine function (AICF) that renders the air gap flux density sinusoidal owing to its asymmetric rotor shape, considering the influence of the armature reaction under the certain load condition. In situations in which the AICF is applied, the average torque is similar but the torque ripple is lower than that of the eccentric rotor shape or the ICF model. In addition, the THD of the induced voltage can be decreased because the saturation distribution in the rotor is balanced under the certain load condition owing to the asymmetric rotor shape. To verify the validity of

Manuscript received March 22, 2017; revised August 6, 2017; accepted September 7, 2017. Date of publication September 20, 2017; date of current version February 16, 2018. This work was supported by the Ministry of Science and ICT, South Korea, under the Information Technology Research Center support program (IITP-2017-2012-0-00628) supervised by the Institute for Information and communications Technology Promotion. Paper no. TEC-00215-2017. *(Corresponding author: Jung-Pyo Hong.)*

The authors are with the Department ofAutomotive Engineering Hanyang University, Seoul 04763 South Korea (e-mail: yhjung207@hanyang.ac.kr; limmang87@hanyang.ac.kr; myunghyoon@hanyang.ac.kr; traik@hanyang.ac.kr; hongjp@hanyang.ac.kr).

Color versions of one or more of the figures in this paper are available online at http://ieeexplore.ieee.org.

Digital Object Identifier 10.1109/TEC.2017.2752753

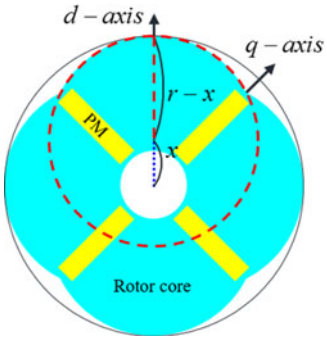

Fig. 1. Principle of eccentric rotor shape.

the AICF method, the torque characteristics and the THD of the induced voltage of the normal model and the model with the AICF are compared using finite element analysis (FEA) under the rated load condition. Moreover, experimental results of the torque characteristics of the normal model and the AICF model are compared.

II. Conventional Methods

The magneto motive force (MMF) generated by the permanent magnets (PMs) and the armature reaction is constant regardless of the shape of the rotor. However, the magnetic field distribution is closely related to the shape. As shown in (1), the MMF is expressed as the product of the reluctance and the magnetic flux.

$$F = R\Phi \tag{1}$$

where F is the MMF; R is the magnetic reluctance; Φ is the magnetic flux. Therefore, the magnetic field distribution can be changed by adjusting the reluctance. Because the reluctance is proportional to the magnetic path length, as shown in (2), the reluctance can be adjusted by changing the length of the magnetic path.

$$R = \frac{l}{\mu_0 \mu_r A} \tag{2}$$

where l is the magnetic path length; μ_0 is the permeability in vacuum; μ_r is the relative permeability of the material; and A is the cross-sectional area of the magnetic path. Therefore, the air gap magnetic field distribution can be made more sinusoidal by adjusting the air gap length appropriately.

A. Conventional Method1: Eccentric Rotor Shape

The use of an eccentric rotor shape [18] is one of the most conventional methods for reducing the torque ripple in the design of electric motors. Using an eccentric rotor shape makes the air gap flux density sinusoidal under a no-load condition. As shown in Fig. 1, if the rotor radius of the original model is r and the eccentric length is x, the radius of the eccentric rotor shape model becomes r-x. This is performed for all the poles. The air gap length on the d-axis becomes a minimum and is the same as the air gap length of the original model. However, the air gap length increases towards the q-axis. Therefore, an eccentric rotor shape should be carefully used in the motor for achieving the required torque and excellent motor characteristics because characteristics such as the cogging torque, the THD of the back electromotive force (BEMF), and the torque ripple of the eccentric rotor shape model vary according to the eccentric length, x [17], [18]. However, if a large eccentric length is applied, the average air gap length increases. In addition, this method does not consider the armature reaction and the saturation distribution under load conditions.

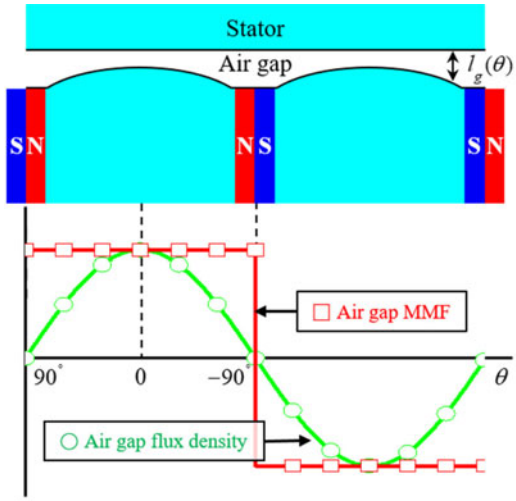

Fig. 2. Air gap MMF and flux density under no-load condition.

B. Conventional Method2: Inverse Cosine Function (ICF)

The ICF calculates the air gap length for maintaining the air gap flux density sinusoidal under a no-load, similar to the eccentric rotor shape model. For using an analytical approach, the permeability of the magnetic core is assumed infinite. In the IPMSM, the MMF of the air gap under a no-load condition is determined only by the MMF of the PM, as shown by red square symbol in Fig. 2. To make the sinusoidal air gap flux density distribution from the rectangular waveform of the MMF, the air gap length should be changed according to the angle, θ. As shown by the green circle symbol in Fig. 2, a sinusoidal air gap flux density can be achieved by adjusting the air gap length using the ICF. The ICF is derived from (3)–(6).

$$\Phi_g = \frac{F_g}{R_g} \tag{3}$$

$$B_g = \frac{\Phi_g}{A_g} = \frac{\mu_0 F_g}{l_g} \tag{4}$$

where Φ_g is the air gap flux; F_g is the air gap MMF; R_g is the air gap reluctance; B_g is the air gap flux density; A_g is the cross-sectional area of the air gap; μ_0 is the permeability of vacuum; and l_g is the air gap length.

Equation (4) can be expressed as the periodic function (5), according to the angle, θ. The range of θ is from $-90°$ ~$90°$ in the electrical angle.

$$B_{\max} \cos\theta = \frac{\mu_0 F_g}{l_g(\theta)} \tag{5}$$

where $B_{\max}$ is the maximum value of the air gap flux density and $l_g(\theta)$ is the air gap length using θ.

The air gap flux density is maximum at the d-axis position, $\theta = 0°$, as shown in Fig. 2. Since the air gap length of d-axis, l_d, is identical to that of the normal model, the maximum air gap flux density can be expressed by (6).

$$B_{\max} = \frac{\mu_0 F_g}{l_d} \tag{6}$$

where l_d is the air gap length of d-axis.

Under no-load condition, the air gap MMF only has the air gap MMF by the PM. The air gap MMF by the PM can be calculated as in (7) according to the Ampere's law, at which, the core permeability is assumed to be infinite.

$$F_g = F_m = \frac{B_r A_m l_m l_g}{\mu_0 \left(\mu_{rec} A_m l_g + A_g l_m\right)} \tag{7}$$

where F_m is the MMF of the PM at the air gap; B_r is the residual induction; A_m is the cross-sectional area of the PM; l_m is the thickness of the PM; l_g is the air gap length; μ_{rec} is the recoil permeability of the PM; A_g is the cross-sectional area of the air gap.

Thus $B_{\max}$ can be derived from (6) and (7). By substituting (6) to (5), the periodic function of the air gap length can be expressed as in (8).

$$l_g(\theta) = \frac{l_d}{\cos\theta} \tag{8}$$

As $-90° < \theta < 90°$, the rotor shape in (8) is symmetrical to the d-axis.

Similar to the eccentric rotor shape model, the ICF can also reduce the cogging torque, the THD of the BEMF, and the torque ripple but can cause a reduction in the average torque owing to the increase in the air gap length. In addition, the ICF do not consider a load condition.

III. Proposed Method: Advanced Inverse Cosine Function (AICF)

The AICF is the equation that adjusts the air gap length by considering the effect of the armature reaction based on the ICF. For the convenience of the analytical approach, the permeability of the magnetic core is assumed infinite. Moreover, it is assumed that the MMF distribution by the armature winding can be considered sinusoidal because only the fundamental component of the air gap MMF is considered in this paper, regardless of the winding method. Fig. 3 is a simplified representation of the air gap MMF, considering the effect of the armature reaction under a certain load condition. As shown in Fig. 3, the red square symbol is the resultant air gap MMF and is the sum of the MMFs of the PM and the armature winding. Consequently, the armature reaction causes a decrease in the resultant air gap flux density under one-half of the pole and an increase in the other half. The AICF enlarges the air gap length of the area where the air gap flux density is increased and reduces the air gap length of the area where the flux density is reduced by the armature reaction. Consequently, the air gap flux density distribution is rendered sinusoidal, as shown in Fig. 4. Thus, the saturation distribution of the rotor core can be well balanced under a load condition.

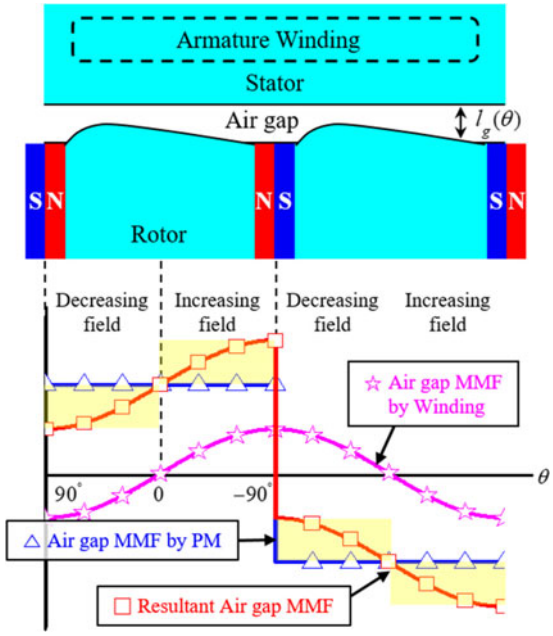

Fig. 3. Air gap MMF distribution considering armature reaction.

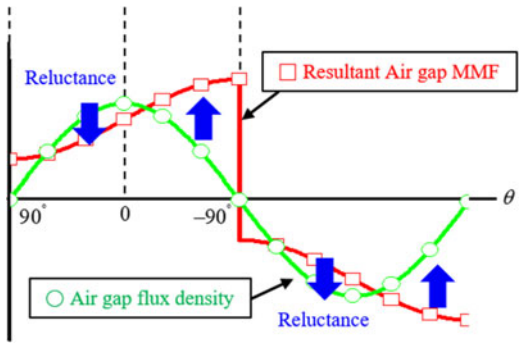

Fig. 4. Air gap MMF and flux density considering armature reaction.

A. Function of Air Gap Length

As seen in Fig. 3, the resultant air gap MMF can be expressed as (9) and is measured from the center of the *N* pole.

$$F_g = F_m - F_w \sin(\theta + \beta) \tag{9}$$

where F_m is the air gap MMF of the PM and F_w is the air gap MMF of the armature current. β is the current phase angle.

Equations (10) and (11) are generated by substituting (9) in (8).

$$l_g(\theta) = \frac{l_d}{\cos\theta} - k_F \frac{l_d \sin(\theta + \beta)}{\cos\theta} \tag{10}$$

where,

$$l_d = \frac{\mu_0 F_m}{B_{\max}} \tag{11}$$

$$k_F = \frac{F_w}{F_m} \tag{12}$$

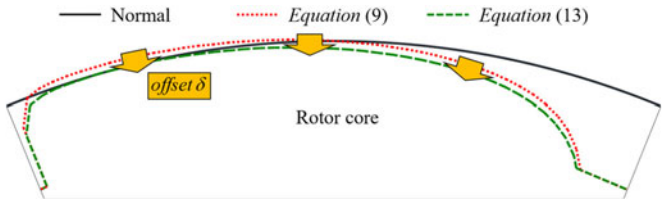

Fig. 5. Rotor shape considering δ offset.

where θ varies from -90 ~90° in the electrical angle and (12) represents the MMF ratio. The first term on the right side of (10) is the air gap length derived from the ICF and the second term is added considering the effect of the armature.

As seen in (10), k_F is an important factor that determines the asymmetric shape of the AICF model and is defined as the ratio of the air gap MMF owing to the PM to the air gap MMF provided by the armature reaction. As k_F increases, the shape of the rotor becomes more asymmetric and the minimum air gap length decreases. Thus, the air gap length of the AICF model is partially reduced when the AICF is applied using (10). Accordingly, a modification in the minimum air gap length (offset δ application) is required to secure mechanical stability and manufacturing tolerance. The offset magnitude of the AICF model is determined to ensure that the minimum air gap length of the AICF model is equal to the air gap length of the normal model. Assuming that the minimum air gap length of the AICF model and the air gap length of the normal model are $l_{\mathrm{g,\,AICF,\,min}}$ and $l_{\mathrm{g,\,normal}}$, respectively, δ can be defined as (13).

$$\delta = l_{\mathrm{g,\,normal}} - l_{\mathrm{g,\,AICF,\,min}} \tag{13}$$

Accordingly, the modified air gap length is determined by offsetting the rotor surface in a radially inward direction by δ, from the rotor shape of the AICF model calculated by (10). Consequently, (10) is changed to (14).

$$l_g(\theta) = \frac{l_d}{\cos\theta} - k_F \frac{l_d \sin(\theta+\beta)}{\cos\theta} + \delta \tag{14}$$

Fig. 5 is an illustration depicting the differences in the rotor shapes with the same k_F using (10) and (14) as an example.

B. Calculation of $\mathrm{k_F}$

To determine k_F, F_m and F_w should be calculated. F_m and F_w can be calculated by using the Ampere's law. It is assumed that the permeability of the magnetic core is infinite. F_m can be calculated using (7) and F_w can be calculated through (15).

$$F_w = 1.5 k_w \frac{\sqrt{2} N_{ph} I_{\mathrm{rms}}}{2pp} \tag{15}$$

where F_w is the MMF of the armature winding at the air gap; k_w is the winding factor; N_{ph} is the series turns per phase; I_{rms} is the *rms* current; and *pp* is the number of pole pairs.

IV. Analysis and Verifications

Under the same current condition, the torque characteristics as well as the induced voltage waveform of the normal and the AICF models are analyzed by FEA. The FEA conducted in the paper is nonlinear, considering the saturation of the magnetic core. In addition, the same current condition is applied to all the four models and a series of magneto-static computations are conducted. As the input current in the paper is assumed sinusoidal, the effect of the pulse width modulation (PWM) is neglected. The angle step for the FEA in the paper is 0.5° and this depicts the tendency of the induced voltage. Harmonic analysis is conducted to obtain the THD of the induced voltage, where sufficient data is obtained by interpolation. Finally, experiments are conducted to verify the validity of the proposed design method and the FEA results.

TABLE I
Model Specification

Quantity	Unit	Value
Pole/slot number	–	8/12
Stator Outer diameter	mm	170
Stator inner diameter	mm	120.7
Air gap length	mm	0.85
Stack length	mm	135
Core material	–	50PN470
Residual induction	T	0.38
Rated speed	rpm	2000
Rated torque	Nm	24
Rated current	$\mathrm{A_{rms}}$	30
Rated Power	kW	5
Drive method	–	$\mathrm{I_d} = 0$ control

A. Proposed Models

In the paper, the normal, the ICF and the AICF models are proposed. All the proposed machines are spoke type IPMSMs, i.e., concentrated flux-type synchronous motors (CFSM) with a permanent magnets arranged diagonally in the rotor core so that the flux density can be maximized by increasing the usage of magnets under the condition of the same rotor outer diameter [21]. Winding type is a concentrated winding and an $\mathrm{I_d} = 0$ control method is used. The core material of the stator and the rotor is an electrical steel sheet, 50PN470. The thickness and the iron loss density of the core material are 0.5 mm and 4.70 W/kg, respectively, when the flux density is 1.5 T at 50 Hz. The number of poles and slots are 8 and 12, respectively. The minimum air gap length is 0.85 mm. The outer diameter and the stack length of the stator are 170 mm and 135 mm, respectively. The residual induction of the PM is 0.38 T. The rated speed is 2000 rpm, and the rated torque and power are 24 Nm and 5 kW, respectively. The specifications are summarized in Table I.

The ICF model is obtained by applying (6). The AICF is applied under the rated load condition of the normal model because the normal model is operated only at that condition. The magnitude and phase angle of the rated current are 30 $\mathrm{A_{rms}}$ and 0° for achieving the rated torque for the normal model. The rotor shape of the AICF model is determined using (13) proposed in this paper, considering the same rated current condition of the normal model. For the determined and presented AICF model, the k_F calculated by (7), (12), and (15) is 0.80, and δ is determined as 0.34 mm. The proposed motors are presented in Fig. 6

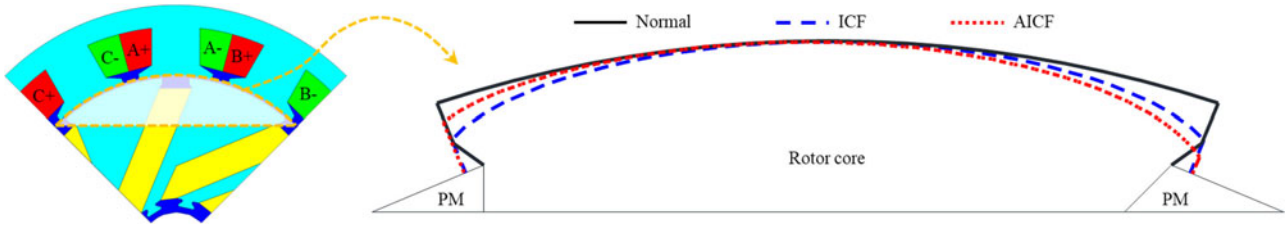

Fig. 6. Configuration of the proposed models.

TABLE II
NO-LOAD BEMF OF THE PROPOSED MODELS

Model	Factor	BEMF (V_{rms})
Normal	–	32.8
ICF	–	31.5
AICF	$k_F = 0.8, \delta = 0.34$ mm	31.3

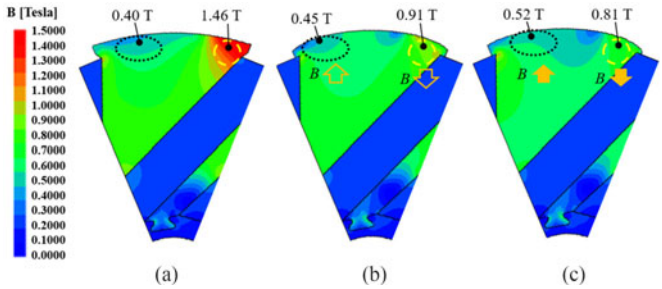

Fig. 7. Magnetic field distribution of the rotor according to mode under the rated load condition. (a) Normal. (b) ICF. (c) AICF.

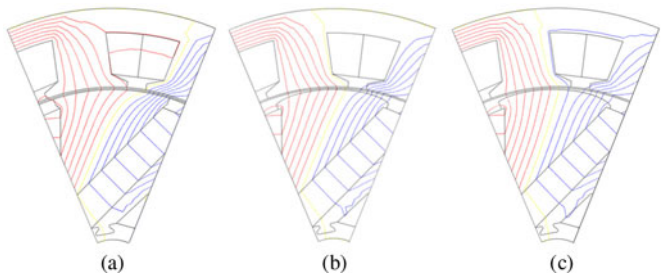

Fig. 8. Flux lines according to the models under the rated load condition. (a) Normal. (b) ICF. (c) AICF.

shows the differences between the rotor shapes of the models. While the normal model has a constant air-gap length, the ICF and AICF model has a different air-gap length according to the angle as shown in Fig. 6.

B. Comparison of the Proposed Models Using FEA

Nonlinear FEA is conducted to verify the design method proposed in the paper. The no-load BEMFs of the proposed models are organized in Table II. Figs. 7 and 8 show the magnetic flux density distributions and the flux lines of the three models under a rated load condition. As shown in Fig. 7, the normal rotor has a high flux density on the right side and a low flux density on the left side, relatively. However, the saturation on the right and left side of the AICF rotor are decreased and increased,

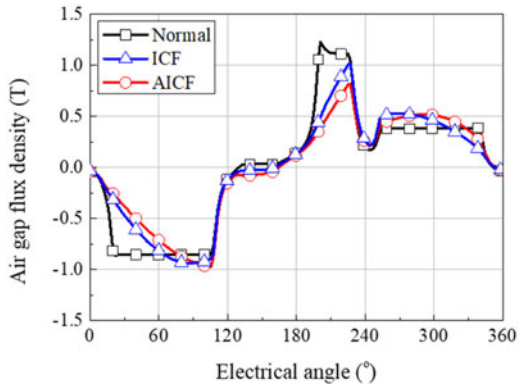

Fig. 9. Air gap flux density waveforms of the three models.

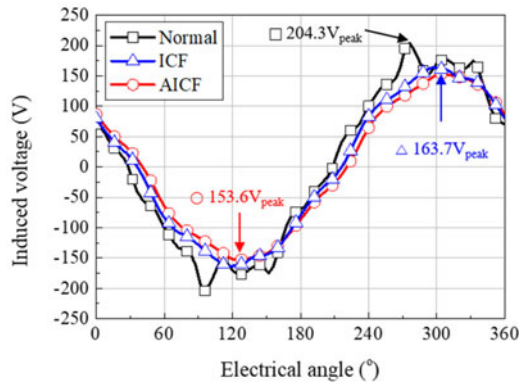

Fig. 10. Induced voltage of three models under the rated load condition.

relatively, in comparison with the normal model. In addition, the variations in the saturation of the AICF rotor are larger than that of the ICF. Thus, the magnetic flux density distribution of the rotor becomes relatively well balanced by applying the AICF. The air gap flux density waveforms of the three models are shown in Fig. 9.

The peak value of the induced voltage is significant. Because the input current is insufficient as the peak value of the induced voltage exceeds the DC link voltage. Consequently, difficulties in controlling the motor and a decrease in the performance occur because the demanded current cannot be input. Thus, the induced voltage of each model under the rated load condition is analyzed, as shown in Fig. 10, where the peak value of the induced voltage of the AICF model is lower than that of the other models under the same load condition. The peak value of the AICF model is 153.6 V and is lower by 24.8% compared to the normal model. Fig. 11 shows the normalized magnitudes

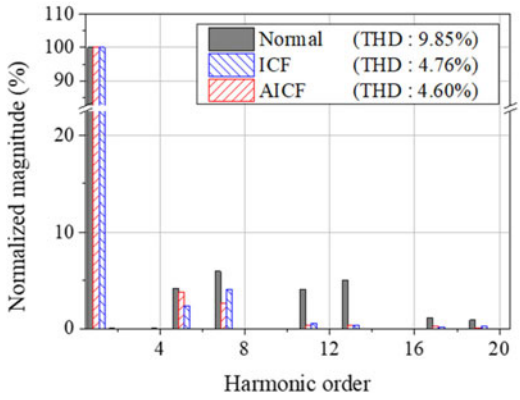

Fig. 11. Harmonic analysis of induced voltage of three models under the rated load condition.

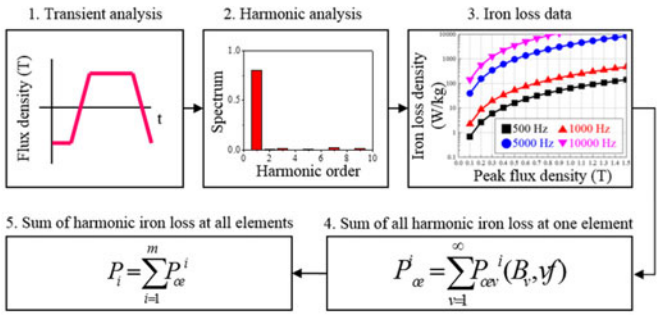

Fig. 12. Calculation process of the iron loss of the motors.

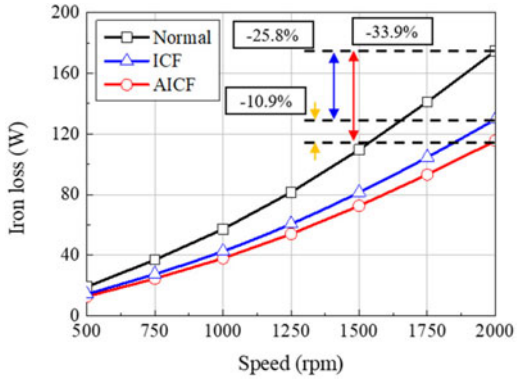

Fig. 13. Iron loss of three models.

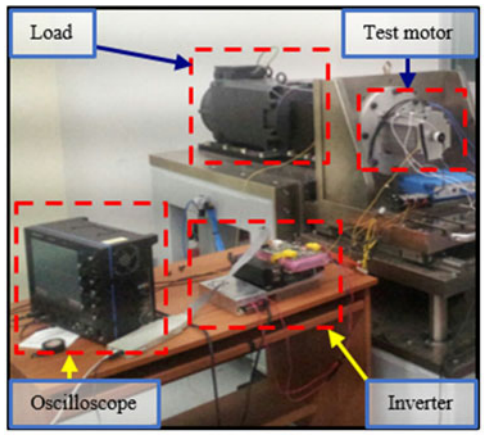

Fig. 14. Experimental setup.

of the fundamental and harmonic components of the induced voltage obtained by fast Fourier transform (FFT). The THD of the induced voltage of the AICF model is 4.60%. The THD value of the AICF model is lower than that of the other models because of the balanced distribution of the magnetic field in the rotor owing to an asymmetric rotor shape obtained by applying the AICF.

To verify the effectiveness of the proposed design method, the iron losses of the two models are analyzed. Fig. 12 shows the process of determining the iron losses, described in detail as follows [22].

1) Step 1: Using the non-linear FEA, the flux density at each mesh for one electrical angle period is calculated, as the rotor is rotated under a load condition. Here, the flux density is calculated as normal and tangential components.
2) Step 2: Using the flux density from Step 1, a Fourier transform is performed to determine the magnitude and phase of the fundamental and harmonic components.
3) Step 3: From the iron loss data of the material, the iron loss corresponding to the frequency and flux density of each harmonic is calculated, considering its phase. The material information is based on empirical data.
4) Step 4: The sum of the iron losses owing to the harmonic components at each mesh is calculated.
5) Step 5: The iron losses of all the meshes are added to determine the total iron loss of the machine.

As shown in Fig. 13, the iron loss of the AICF model is also reduced because of the balanced saturation distribution. The iron loss of the AICF model, 115.4 W, is lower than that of the other models because the harmonic components of the rotor magnetic field distribution are reduced. As the iron loss increases with the operating speed, the differences in the iron loss between the AICF and the other models increase. Therefore, the increment in the efficiency of the AICF model in comparison with the other models is higher as the operating speed increases.

C. Verifications

Finally, the average torque and torque ripple of the normal and AICF model are compared. In order to validate the proposed design method and FEA results, the experiments are conducted at intervals of 10 A_{rms} from 10 A_{rms} to 60 A_{rms}. During the experiment, the test motor is connected in series with the load, mechanically, through a torque sensor. The load is a 50 kW induction motor and the torque sensor is a 4503A type of KISTLER. The measurement range of the torque sensor used in this study is $0 \sim 100$ Nm according to the options, and the maximum error is 0.2%. With the use of an oscilloscope, the torque waveform is identified on receiving a signal from the torque sensor; LeCroy WaveRunner 64 Xi is used as the oscilloscope. Figs. 14 and 15 show the experimental setup and photos of the manufactured motors, respectively. The average torque and torque ripple according to the various load condition is shown in Fig. 16. As shown in Fig. 16(b), the torque ripple of the AICF model is

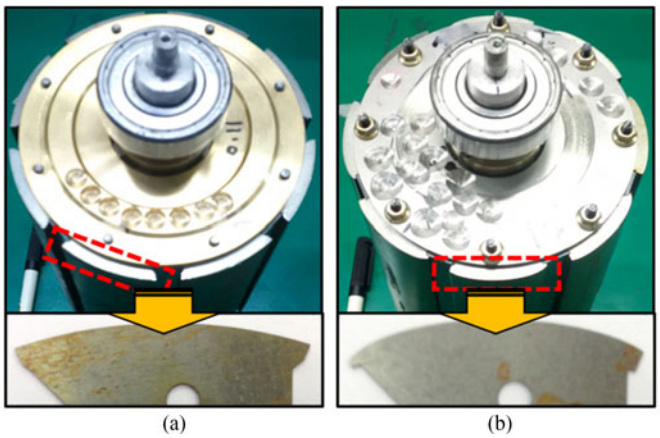

Fig. 15. Manufactured rotors. (a) Normal. (b) AICF.

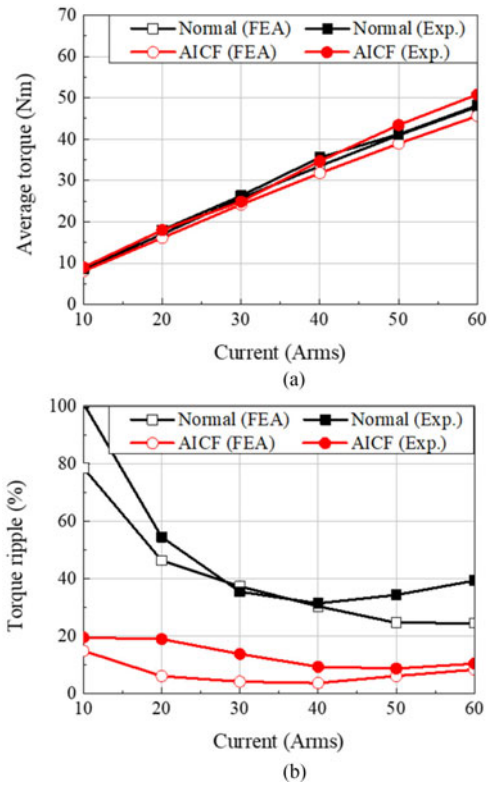

Fig. 16. Average torque and torque ripple of the FEA and experiment according to the current magnitude. (a) Average torque. (b) Torque ripple.

the lowest compared to the other model under all the current conditions. Table III shows the torque characteristics under the rated load condition. The average torque of the AICF model is similar to that of the normal model. The torque ripple of the AICF model is the lower than the normal model under the rated load conditions. The torque ripple of the AICF model is reduced by 33.1% in FEA compared to the normal model under the rated load conditions. Likewise the torque ripple of the AICF model is lower by 21.7% than that of the normal model in the experiment. The torque wave of the proposed models under the rated load condition is shown in Fig. 17. The average torque is slightly different but it can be verified that the torque waveforms of the results of the FEA and the experiment are similar.

TABLE III
TORQUE PERFORMANCE UNDER THE RATED LOAD CONDITION

Model	Model	Average torque (Nm)	Torque ripple (%)
Normal	FEA	25.7	37.3
	Experiment	26.3	35.5
AICF	FEA	24.2	4.2
	Experiment	24.9	13.8

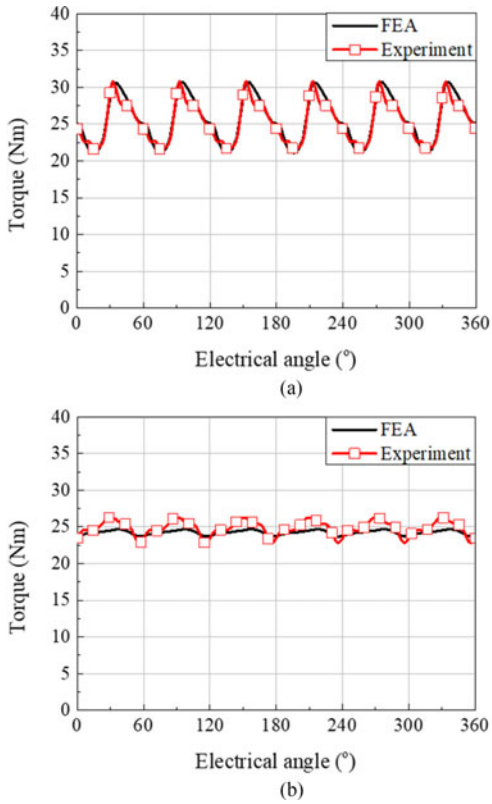

Fig. 17. Torque wave of the FEA and experimental result under the rated load condition. (a) Normal. (b) AICF.

It can be concluded that the design method using the AICF is effective not only for the torque ripple reduction but also for the improvement of the control performance of the electric machines owing to the decreased peak value and the THD of the induced voltage. Further, the iron loss can be reduced in the high-speed region and the efficiency can be increased as a result.

V. CONCLUSION

This paper proposes the use of the AICF that renders the air gap flux density sinusoidal, considering the armature reaction under the rated load condition. The air gap length and the rotor shape have been determined based on the current magnitude and the current phase angle, and an asymmetric shape is used because of the armature reaction. In the case of the AICF model, the torque ripple is significantly reduced compared to the normal model. In addition, the peak value and THD of the induced voltage of the AICF model are lower than those of the other models because the magnetic field distribution of the rotor in the AICF model is relatively well balanced owing to the asymmetric rotor shape. In addition, the iron loss of the AICF model is reduced

because of the balanced magnetic field distribution. As a result, the THD of the induced voltage and the iron loss of the AICF model can be decreased by 5.25% and 33.90%, respectively, compared to those of the normal model under the rated load conditions. In order to verify the validity of the proposed design method and the FEA results, load experiments were conducted. The average torque, torque ripple, and the torque waveforms of the experimental results are similar to those of the FEA results. Thus, the proposed design method using the AICF is effective in improving the torque characteristics, the control performance, and reducing the iron loss.

REFERENCES

[1] K. I. Laskaris and A. G. Kladas, "Interior permanent magnet motor design for electric vehicle drive," *IEEE Trans. Ind. Electron.*, vol. 57, no. 1, pp. 138–145, Jan. 2010.

[2] J. F. Gieras, C. Wang, and J. C. Lai, "Torque pulsuation," in *Noise of Polyphase Electric Motors*, 1st ed. Boca Raton, FL, USA: CRC Press, 2006, ch. 4, pp. 77–105.

[3] P. Beccue, J. Neely, S. Pekarek, and D. Stutts, "Measurement and control of torque ripple-induced frame torsional vibration in a surface mount permanent magnet machine," *IEEE Trans. Power Electron.*, vol. 20, no. 1, pp. 182–191, Jan. 2005.

[4] K. Wang, Z. Y. Gu, Z. Q. Zhu, and Z. Z. Wu, "Optimum injected harmonics into magnet shape in multiphase surface-mounted PM machine for maximum output torque," *IEEE Trans. Ind. Electron.*, vol. 64, no. 6, pp. 4434–4443, Jun. 2017.

[5] W. Qian, S. K. Panda, and J.-X. Xu, "Torque ripple minimization in PM synchronous motors using iterative learning control," *IEEE Trans. Power Electron.*, vol. 19, no. 2, pp. 272–279, Mar. 2004.

[6] P. Zhang, G. Y. Sizov, and N. A. O. Demerdash, "Comparison of torque ripple minimization control techniques in surface-mounted permanent magnet synchronous machines," in *Proc. Conf. Int. Elect. Mach. Drives*, May 2011, pp. 188–193.

[7] Y. Cho, K.-B. Lee, J.-H. Song, and Y. I. Lee, "Torque-ripple minimization and fast dynamic scheme for torque predictive control of permanent-magnet synchronous motors," *IEEE Trans. Power Electron.*, vol. 30, no. 4, pp. 2182–2190, Apr. 2015.

[8] H. Lu, L. Zhang, and W. Qu, "A new torque control method for torque ripple minimization of BLDC motors with un-ideal back EMF," *IEEE Trans. Power Electron.*, vol. 23, no. 2, pp. 950–958, Mar. 2008.

[9] Z. Q. Zhu and D. Howe, "Influence of design parameters on cogging torque in permanent magnet machines," *IEEE Trans. Energy Convers.*, vol. 15, no. 4, pp. 407–412, Dec. 2000.

[10] G.-H. Kang, Y.-D. Son, G.-T. Kim, and J. Hur, "A novel cogging torque reduction method for interior-type permanent-magnet motor," *IEEE Trans. Ind. Appl.*, vol. 45, no. 1, pp. 161–167, Jan./Feb. 2009.

[11] T. Ishikawa, M. Yamada, and N. Kurita, "Design of magnet arrangement in interior permanent magnet synchronous motor by response surface methodology in consideration of torque and vibration," *IEEE Trans. Magn.*, vol. 47, no. 5, pp. 1290–1293, May 2011.

[12] S.-I. Kim, J.-Y. Lee, Y.-K. Kim, J.-P. Hong, Y. Hur, and Y.-H. Jung, "Optimization for reduction of torque ripple in interior permanent magnet motor by using the Taguchi method," *IEEE Trans. Magn.*, vol. 41, no. 5, pp. 1796–1799, May 2005.

[13] Y. Kano, T. Kosaka, N. Matsui, and T. Nakanishi, "A new technique of torque ripple reduction in saliency-based sensorless drive IPM motors for general industrial applications," in *Proc. 13th Eur. Conf. Power Electron. Appl.*, Sep. 2009, pp. 1–10.

[14] J.-W. Jung, S.-H. Lee, G.-H. Lee, J.-P. Hong, D.-H. Lee, and K.-N. Kim, "Reduction design of vibration and noise in IPMSM type integrated starter and generator for HEV," *IEEE Trans. Magn.*, vol. 46, no. 6, pp. 2454–2457, Jun. 2010.

[15] X. Ge, Z. Q. Zhu, G. Kemp, D. Moule, and C. Williams, "Optimal step-skew methods for cogging torque reduction accounting for three-dimensional effect of interior permanent magnet machines," *IEEE Energy Convers.*, vol. 32, no. 1, pp. 222–232, Mar. 2017.

[16] W. Q. Chu and Z. Q. Zhu, "Investigation of torque ripples in permanent magnet synchronous machines with skewing," *IEEE Trans. Magn.*, vol. 49, no. 3, pp. 1211–1220, Mar. 2013.

[17] P. Zheng, J. Zhao, J. Han, J. Wang, Z. Yao, and R. Liu, "Optimization of the magnetic pole shape of a permanent-magnet synchronous motor," *IEEE Trans. Magn.*, vol. 43, no. 6, pp. 2531–2533, Jun. 2007.

[18] Y. Zhou, H. Li, G. Meng, S. Zhou, and Q. Cao, "Analytical calculation of magnetic field and cogging torque in surface-mounted permanent-magnet machines accounting for any eccentric rotor shape," *IEEE Trans. Ind. Electron.*, vol. 62, no. 6, pp. 3438–3447, Jun. 2015.

[19] S. A. Evans, "Salient pole shoe shapes of interior permanent magnet synchronous machines," in *Proc. 19th Int. Conf. Elect. Mach.*, Sep. 2010, pp. 1–6.

[20] K. Wang, Z. Q. Zhu, G. Ombach, and W. Chlebosz, "Optimal rotor shape with third harmonic for maximizing torque and minimizing torque ripple in IPM motors," in *Proc. 20th Int. Conf. Elect. Mach.*, Sep. 2012, pp. 397–403.

[21] H.-J. Kim, D.-Y. Kim, and J.-P. Hong, "Structure of concentrated-flux-type interior permanent-magnet synchronous motors using ferrite permanent magnets," *IEEE Trans. Magn.*, vol. 50, no. 11, Nov. 2014, Art. no. 8206704.

[22] M. S. Lim, S. H. Chai, J. S. Yang, and J. P. Hong, "Design and verification of 150 krpm PMSM based on experiment results of prototype," *IEEE Trans. Ind. Electron.*, vol. 62, no. 12, pp. 7827–7836, Dec. 2015.

Young-Hoon Jung received the Bachelor's degree in mechanical engineering in 2013, from Hanyang University, Seoul, South Korea, where he is currently working toward the Ph.D. degree in automotive engineering. His research interests include electric machine design for automotive and robot applications and ultrahigh speed motors.

Myung-Seop Lim received the Bachelor's degree in mechanical engineering from Hanyang University, Seoul, South Korea, in 2012, and the Ph.D. degree in automotive engineering from the same university, in 2017. Since 2017, he has been working in Hyundai Mobis, Seoul, South Korea. His research interests include electric machine design for automotive and robot applications and sensorless drive.

Myung-Hwan Yoon received the Bachelor's degree in mechanical engineering in 2011, from Hanyang University, Seoul, South Korea, where he is currently working toward the Ph.D. degree in automotive engineering. His research interests include analysis, design, and optimization of electric machine and numerical analysis of electromagnetic.

Jae-Sik Jeong received the Bachelor's degree in electrical engineering in 2011, from Myongji University, Seoul, South Korea, where he is currently working toward the Ph.D. degree in automotive engineering. His research interests include electric machine design for automotive and robot applications and nonrare earth magnet motor.

Jung-Pyo Hong (SM'97) received the Ph.D. degree in electrical engineering from Hanyang University, Seoul, South Korea, in 1995. From 1996 to 2006, he was a Professor in Changwon National University, Changwon, South Korea. Since 2006, he has been working as a Professor in Hanyang University. His research interests include the design of electric machines, optimization, and numerical analysis of electromechanics.